Efficient Phasor-Based Dynamic Volt/VAr and Volt/Watt Analysis of Large Distribution Grid with High Penetration of Smart Inverters

Maryam Mahmoudi Koutenaei, *Student Member, IEEE*, Thai-Thanh Nguyen, *Member, IEEE*, Tuyen Vu, *Member, IEEE*, Sumit Paudyal, *Member, IEEE*, and Rob Hovsapian, *Senior Member, IEEE*

***Abstract*—As the penetration of power-electronics based smart inverters (SIs) is increasing in distribution grids, it adds computational challenges in solving dynamic models of large-scale distribution feeders. Voltage and reactive power (Volt/VAr), and voltage and active power (Volt/Watt) dynamics have been analyzed at slower time scales akin to the control of legacy grid devices. However, smart inverters, being power-electronics based devices, can provide dynamic active/reactive power support at a faster time scale, which necessitates Volt/VAr and Volt/Watt dynamics to be analyzed at a faster time scale. The existing dynamic models are overly detailed and computationally intractable for distribution feeders with a large number of inverters. In this context, this proposed work aims towards developing a computationally tractable, scalable, and accurate phasor-based model for dynamic Volt/VAr and Volt/Watt analyses of large distribution systems with high penetration of smart inverters. Case studies demonstrate that the proposed phasor-based model sufficiently captures the Volt/VAr and Volt/Watt dynamics, and is computationally faster by one order of magnitude compared to the average model and by two orders of magnitude compared to the detailed switching model. Case studies also demonstrate the efficacy and scalability of the proposed model in analyzing Volt/VAr and Volt/Watt dynamics of large-scale power networks with hundreds of SIs.**

***Index Terms*—Smart inverters, Distribution systems, Dynamic analysis, Volt/VAr control.**

I. Introduction

THE number of solar photovoltaic (PV) installations in US has reached 2 million with capacity over 70 GW. By 2024, 2.5% of US households will have PV inverters installed on their premises [1]. Given the increasing penetration of residential-level inverters on distribution systems and novel grid services the inverters can provide to distribution system operations, several jurisdictions now mandate installation of smart inverters with novel functionalities and communication capabilities (e.g., 'CA Rule 21' and 'HI Rule 14'), which are also emphasized on the IEEE-1547 [2]. Pacific Gas and Electric Company forecasts that 50% residential-scale PV in California will be equipped with smart inverters by 2021, which will increase to 100% by 2028 [3].

This work is supported by National Science Foundation (NSF) grant ECCS-2001732. M. M. Koutenaei and S. Paudyal are with Florida International University, Miami, FL, USA; T. T. Nguyen and T. Vu are with Clarkson University, Potsdam, NY, USA; R. Hovsapian is with the National Renewable Energy Laboratory, Golden, CO, USA. Emails: mmahm024@fiu.edu, tnguyen@clarkson.edu, tvu@clarkson.edu, spaudyal@fiu.edu, rob.hovsapian@nrel.gov. Corresponding Author: S. Paudyal, Email: spaudyal@fiu.edu

In future distribution grids, novel grid applications can be achieved through the coordination of smart inverters [4]. One of such applications includes voltage and reactive power (Volt/VAr) support by the inverters. To enable voltage and reactive power control from the smart inverters, IEEE-1547 mandates several rules including that the smart inverters to be capable of consuming or producing reactive power when inverters are at or above 5% of their rated active power, and mandatory active power curtailment regions [2]. Conventionally, Volt/VAr regulation has been achieved through the control of legacy grid devices (e.g., load tap changers and switched capacitors) [5], which can now be achieved through the control of power-electronics based smart inverters. The controller of smart inverters is typically based on the cascaded control architecture, which includes the inner current control loop and outer voltage or power control loop [6]. Since the control loops in the inverters operate at much faster time scale compared to that of load tap changers and capacitor banks, the conventional quasi-steady-state power-flow based method [7], [8] in controlling the legacy grid devices for Volt/VAr regulation will not suffice to capture the voltage and reactive power dynamics of the smart inverters. Therefore, the grid operators require efficient and scalable models and methods to analyze faster time-scale Volt/VAr and Volt/Watt dynamics of distribution grids with smart inverters.

A detailed switching model would indeed capture the necessary dynamics of smart inverters for voltage and reactive power control but at exceptionally high computational burden. Existing average inverter models in literature [9], which ignore the switching dynamics, are also computationally burdensome for a large number of inverters. For example, a 10-second simulation of a single PV model takes 3.5 minutes using switching model, while it takes 1.25 minutes using the average model [10]. A recent work on real-time simulation of inverter-rich power grid showed that four CPU cores (3.56 GHz speed) with the sampling time of 50 μs can simulate up to 40 average inverter models [11]. These studies [10], [11] clearly showed that neither the switching model nor the average model are computationally tractable for large distribution feeders with 100's of distributed smart inverters.

There are recent attempts in developing reduced order differential-algebraic equations (DAE) of the inverters connected to distribution feeder to ease the computational burden [12]. Model reduction of inverters based on singular perturbation was proposed in [13], in which a reduced order

model was obtained by neglecting the fast dynamic state variables. In [14], a reduced-order model of inverters was obtained by using lumped parameters and power scaling laws, which would aggregate multiple parallel inverters as a single inverter. However, the aggregation of inverters would omit the control interaction among them. In addition, those models [12]–[14] consider frequency dynamics that is combined with the voltage dynamics of the inverters, and also the computational burden of those models in solving distribution networks with a large number of inverters is not known. Dynamic phasor modeling is a promising technique for reducing the computation burden as it maintains accurate simulations with larger time steps. The dynamic phasor based modeling of inverters was proposed in [15], [16] for transient analysis, which showed good accuracy to capture the transients and the reduction of simulation time. Dynamic phasor based approach to model simplified inverter dynamics is proposed in [17]. However, the models in [15]–[17] also combine frequency and voltage dynamics. For efficient computational models solely for Volt/VAr dynamic analysis and Volt/VAr control purposes, frequency dynamics need not be considered as the interaction between frequency dynamics and voltage dynamics is minimal. On the other hand, the simplified current injection (source) based approach, as used in slow time-scale quasi-steady-state simulations [7], does not capture any voltage dynamics, particularly during under-voltage and over-voltage ride-through events which last up to ≈20 seconds [2]. Moreover, faster voltage dynamics arising from a few of the control modes as defined in the IEEE-1547 (e.g., dynamic reactive power control) are also not captured through the slow time-scale quasi-steady-state simulations.

To this end, a recent work by Pacific Northwest National Laboratory (PNNL) is very relevant and employs phasor-based power flow solver (GridLAB-D) and integrates simplified inverter dynamic model to GridLAB-D [18], which is an acceptable approach for Volt/VAr dynamic analysis of inverters with a single frequency of interest. The phasor-based voltage dynamic analysis is also justifiable based on the local droop control rules defined in the IEEE-1547 [2], which requires control of reactive power/ reactive current based on local voltage averaged over a couple of cycles. However, the errors obtained in [18] as compared to detailed switching model of inverters, particularly for grid-following mode, are large. Moreover, the solution time for a feeder with only 13 inverters, though the distribution circuit is large, takes up to 30 minutes for a 15-second simulation [18]. As pointed out in [18], the power flow of the underlying power network using off-the-shelf GridLAB-D solver takes significant computation time. Therefore, there is still a research gap and need to develop efficient and scalable phasor-based model of smart inverters for dynamic Volt/VAr and Volt/Watt analysis connected to power distribution network. In this context, contributions of this work are as,

- Development of an efficient and accurate simplified phasor-based model for the analysis of fast time-scale Volt/VAr and Volt/Watt dynamics of smart inverters connected to power distribution systems. Unlike the switching, average, and other reduced order models of the inverters in literature [9], [12], [15]–[17], our proposed model is computationally tractable to large distribution systems with 100's of distributed smart inverters, and sufficiently captures the fast Volt/VAr and Volt/Watt dynamics that would not be possible with slow time-scale quasi-steady-state [7] Volt/VAr simulation approach.
- Validation and applicability of the proposed model compared to the switching and the average models of the inverters for voltage ride-through events and demonstration of the scalability of the proposed modeling approach on the large-scale distribution feeder.

The rest of this paper is arranged as follows. Section II describes the typical configuration of the smart inverter-based PV system. Section III presents the existing detailed and average models of PV systems. Section IV describes the proposed phasor-based model of smart inverter for large-scale system study. Section V discusses the validation of the proposed model. The large-scale simulation is discussed in Section VI. The main contributions of this paper are summarized in Section VII.

II. Overall Configuration and Control of Photovoltaic Systems

Typical configuration of smart inverter-based photovoltaic (PV) system is shown in Fig. 1 [19]. A single-phase two-stage inverter, which consists of a DC/DC boost converter and a DC/AC grid-side converter, is used to connect PV array to the utility grid. The boost converter increases the DC voltage to higher level required by the grid-connected DC/AC converter. DC-side LC-filter and the output LCL-filter are employed to filter the switching frequency ripples caused by boost converter and DC-AC inverter.

A. Photovoltaic Array Model

The PV array in Fig. 1 is modeled through the single-diode PV model. The current-voltage (I_{PV} - V_{PV}) relationship of a single PV module is presented as [20],

$$I_{PV} = I_{ph} - I_0\left[\exp\left(\frac{V_{PV}+I_{PV}R_s}{N_cV_T}\right)-1\right]-\frac{V_{PV}+I_{PV}}{R_{sh}} \quad (1)$$

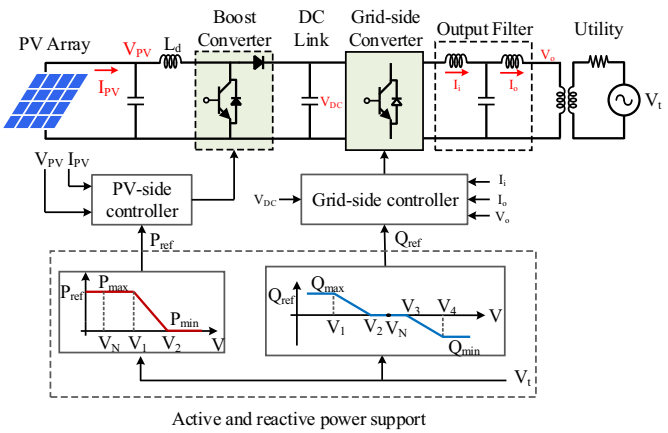

Fig. 1. Typical configuration and control of PV system [19], with active and reactive power support function as per the IEEE-1547.

where N_c is the number of series cells in the module; R_s and R_{sh} are the series resistance and shunt resistance; I_{ph} is the photo current; I_0 is the diode saturation current; V_T is the thermal voltage expressed through $V_T = kAT/q$, where k is the Boltzmann's constant; q is the electron charge and A is the diode ideality factor which is a small number close to 1. The parameters I_{ph}, I_0, R_{sh}, and R_s are estimated for standard test condition (STC) which are given in Table I. Then, the only parameters which are considered to change with irradiance and temperature are I_0 and I_{ph}, and are updated through (2) and (3) respectively [20] as,

$$I_0 = I_{0,STC}\left[\frac{T}{T_{STC}}\right]^3 \exp\left(\frac{qE_g}{Ak}\left(\frac{1}{T_{STC}} - \frac{1}{T}\right)\right) \quad (2)$$

$$I_{ph} = \left(I_{ph,STC} + k_i \Delta T\right) G \quad (3)$$

where $T_{STC} = 273.15\,\text{K}$ is the temperature at STC; $E_g = 1.1\,\text{eV}$ is the silicon bandgap energy; k_i is the short circuit current temperature coefficient; and and G is the irradiance ratio.

B. Control Configuration

The overall control diagram of the smart inverter is also shown in Fig. 1, which consists of PV-side controller, grid-side controller, and active/reactive powers support functions (as per the IEEE-1547 [2]). The PV system works in four different control modes. The default control mode is the unity power factor or Maximum Power Point Tracking (MPPT) mode. Another control mode is constant reactive power, where the reactive power reference Q_{ref} can be tuned locally or remotely [2]. Since the IEEE-1547 requires smart inverters to have both active and reactive power control capabilities during the normal operation, the active power support function (Volt-Watt) and reactive power support function (Volt-VAr) as shown in Fig. 1 are implemented in the control configuration of the smart PV inverter. The reactive power reference Q_{ref} in the Volt-VAr mode and the target set-point of PV power P_{ref} in the Volt-Watt mode are functions of the smart inverter output voltage following the IEEE-1547 default droop settings [2]. During reactive power priority modes, including constant reactive power and Volt-VAr modes, the set-point P_{ref} for active power curtailment is obtained by (4) to meet the inverter apparent power limit, i.e., S_{rated}.

$$P_{ref} = \sqrt{S_{rated}^2 - Q_{ref}^2} \quad (4)$$

With the PV-side controller, the maximum power extraction of the PV array (P_{PV}) can always be achieved by the MPPT mode. In addition, P_{PV} can be reduced to the set-point (P_{ref}) when the Constant Power Generation (CPG) mode is activated in the Volt-Watt mode or active power curtailment needed in other control modes. In this regard, the PV-side controller operation based on P_{ref} is given by as,

$$P_{PV} = \begin{cases} P_{MPPT}, & \text{when } P_{PV} \le P_{ref}, \\ P_{ref}, & \text{when } P_{PV} > P_{ref}. \end{cases} \quad (5)$$

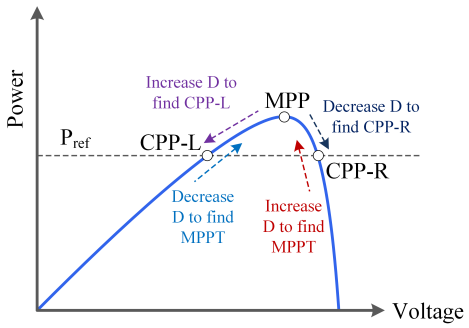

Fig. 2. Operating mode of PV-side controller [23].

The perturb and observe algorithm (P&O) is used in this work for both the MPPT and CPG modes [21]–[23]. During the MPPT mode, the P&O algorithm is executed to directly find the optimal duty cycle (D) of the boost converter whereas in the CPG mode the P&O algorithm directly calculates D to regulate the PV power to the target set-point P_{ref}. As shown in Fig. 2, there are two operation areas of the CPG modes, which are the right side (CPP-R) of the maximum power point (MPP) and the left side of MPP (CPP-L). However, for the two-stage PV system used in this paper, the PV output power is regulated at the CPP-L to achieve stable CPG operation [22].

The main functions of the grid-side controller are to regulate the output reactive power of the smart inverter and control the DC-link voltage to ensure constant active power flow to the grid-side converter.

III. Existing Models of the PV System

Existing models of PV systems used for simulation purposes include detailed and average models. The difference between those models is the converter modelling and control; however, the active and reactive power support functions remain the same. The detailed model can represent the accurate behavior of PVs including harmonics but it is computationally intractable. The average model can provide similar behavior and accurate dynamic response compared to the detailed model.

A. Detailed Switching Model

The detailed model uses the switching devices for the DC/DC PV-side converter and DC/AC grid-side converter [24]. The PV-side and grid-side control diagram of the detailed switching converter is shown in Fig. 3. The grid-side converter is responsible for the regulation of DC-link voltage and managing output reactive power of smart inverter. The DC-link voltage and reactive power controllers generate dq current references for the inner current control loop. The dq components of single-phase current and voltage are obtained by using (6), in which the phase angle (ωt) of utility grid voltage is given by the single-phase phase-locked loop (PLL) block, as shown in Fig. 3, in which the "mean" block computes the mean value of the input voltage over one cycle window of the fundamental frequency.

$$\begin{bmatrix} f_d \\ f_q \end{bmatrix} = \begin{bmatrix} \cos(\omega t) & \sin(\omega t) \\ -\sin(\omega t) & \cos(\omega t) \end{bmatrix} \begin{bmatrix} f_\alpha \\ f_\beta \end{bmatrix}. \quad (6)$$

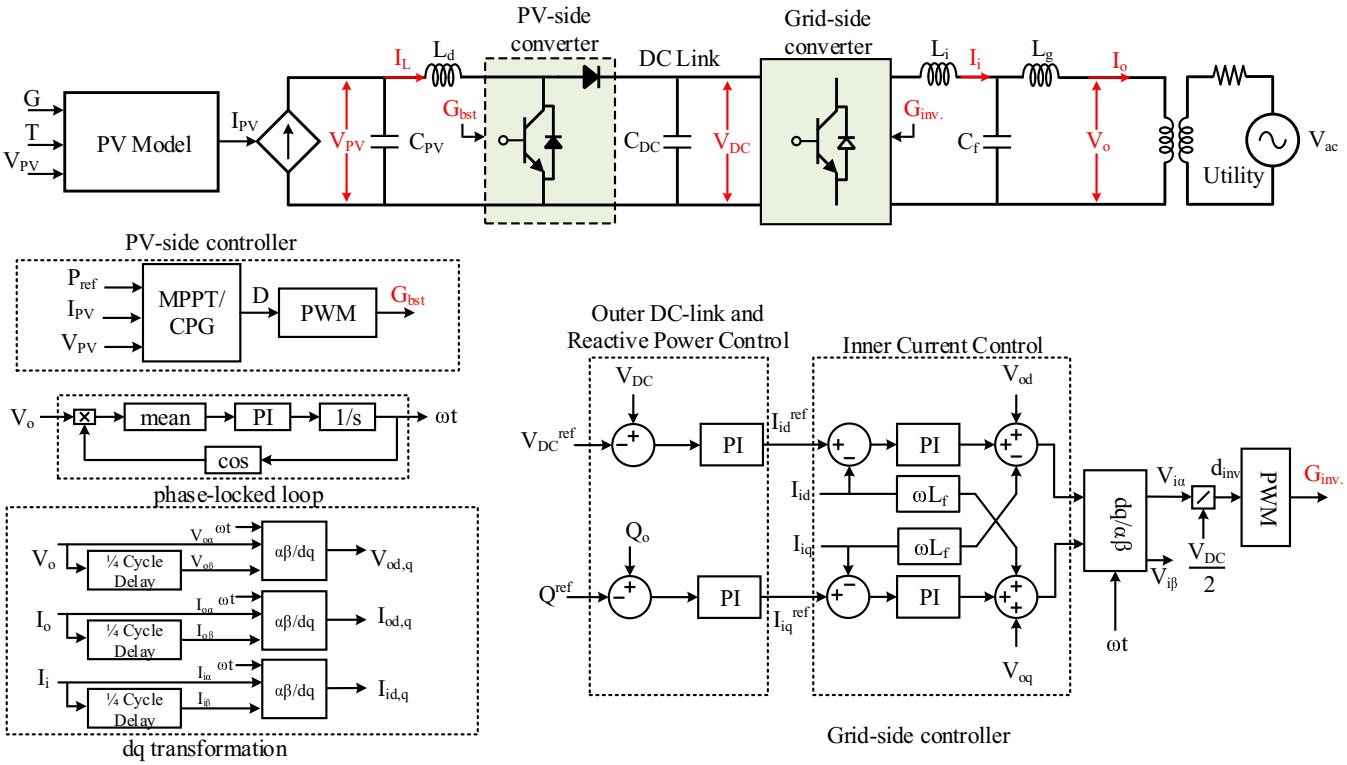

Fig. 3. Detailed model of smart inverter.

where f_α and f_β are the real and imaginary parts of the single-phase signal, in which the real part f_α is the original signal and the imaginary part f_β is obtained by shifting the original signal by 90°. The fixed 90° phase shift between real and imaginary parts is constructed by a quarter-cycle delay [25]. Adopting dq reference frame of an individual inverter as presented in [26], dq components of the output voltage are set as $V_{oq} = 0$ and $V_{od} = |v_o|$, and the output powers of PV system are obtained as,

$$P_o = \frac{V_{od} I_{od}}{2} \tag{7}$$

$$Q_o = -\frac{V_{od} I_{oq}}{2} \tag{8}$$

The proportional-integral (PI) regulators are used to compensate for the errors. The duty cycle is generated by the inner current loop to regulate the inverter current to follow the references. The pulse width modulation (PWM) uses the duty cycle as the input to provide the switching signals for the converters.

B. Average Model

The switching devices in the two-stage control are replaced with their equivalent average models as in [24], [27]. The mathematical model of the boost converter, which operates in continuous-conduction mode (CCM), and the full-bridge inverter are written as,

$$C_{PV} \frac{dV_{PV}}{d_t} = I_{PV} - I_L \tag{9}$$

$$L_d \frac{dI_L}{d_t} = V_{PV} - (1 - D) V_{DC} \tag{10}$$

$$L_i \frac{dI_i}{d_t} = d_{inv} V_{DC} - V_{Cf} \tag{11}$$

$$C_{DC} \frac{dV_{DC}}{d_t} = (1 - D) I_L - d_{inv} I_i \tag{12}$$

where V_{PV} and I_{PV} are PV array voltage and current. C_{PV} and L_d are DC-side LC filter capacitor and inductor. I_L and V_{DC} are boost converter current and DC-link voltage. L_i and I_i are the LCL filter inductor and its current. V_{Cf} is the voltage across the LCL filter capacitor. D and d_{inv} are the duty cycle of boost converter and full-bridge inverter, respectively. Based on (9)- (12), the average model of the PV system can be derived as shown in Fig. 4. The control diagram of the average model is the same as the detailed model except that average model does not have PWM modules. Thus, this model retains all dynamics of the detailed model except for the fast dynamics related to switching devices and PWM modules.

IV. Proposed Phasor-Based Model

Although the average model of the PV system is much faster than the detailed model, it is still computationally burdensome for simulating a large number of distributed PVs connected to distribution feeders. Therefore, to achieve computational efficiency, first, fast dynamics of the inner control loops and DC-side harmonic filter are removed keeping the slower dynamics and LCL filter dynamics on the proposed phasor-based model (see Fig. 5). Please note that removing fast states may lead to modeling errors when compared to the detailed switching-based model; however, the validation carried out in Section V-A shows that the responses from phasor-based model compared to the switching models are fairly accurate as the error is not significant.

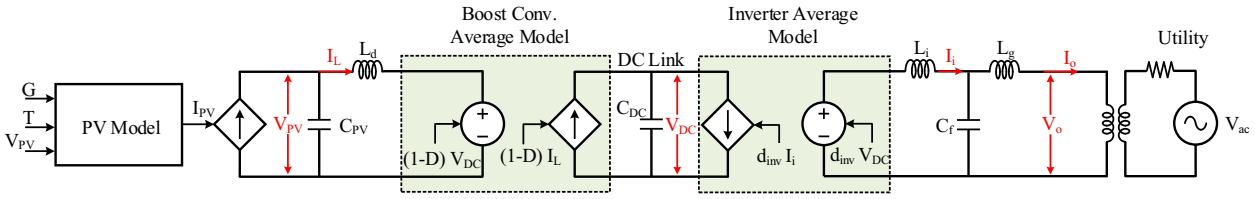

Fig. 4. Average model of inverters.

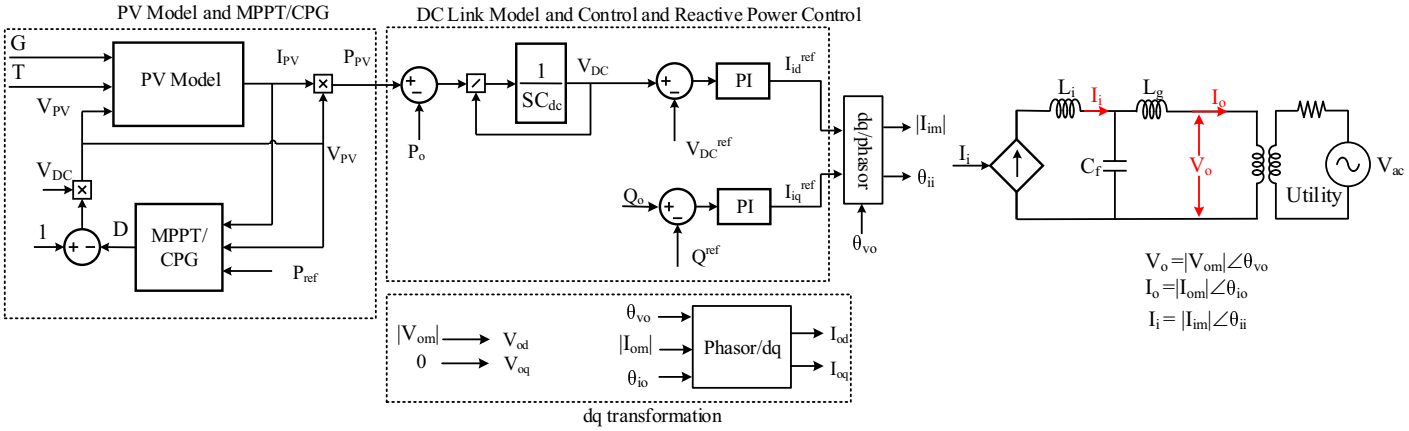

Fig. 5. The proposed phasor-based model.

Next, the PLL block is removed as the phasors of the current and voltage signals of the system are obtained directly at the fundamental grid frequency; thus, there is no need to sense the phase angle of the utility grid voltage (ωt). Moreover, the dq transformation in (6) is replaced with the phasor to dq transformation.

A. Removing Fast Dynamics

To design the control loops of the smart PV inverter, a reasonable bandwidth allocation between the inner (fast) loops and outer (slow) loops are generally considered [28]. Therefore, first, the inner current loops (which exhibit faster dynamics) are removed. Then, the inverter is modeled as a controlled current source whose dq components of currents (I_{id} and I_{iq}) are equal to their references (I_{id}^{ref} and I_{iq}^{ref}) obtained from the DC-link voltage and reactive power control loops. The DC-link capacitor which has slow dynamic is kept to maintain the dynamic interaction between the grid-side converter and PV-side converter. Moreover, since the DC-side LC filter of the system have been designed with high cut-off frequency to remove the switching ripples of the boost converter, it is ignored in the proposed model, which results in following.

$$V_{PV} = (1 - D)\, V_{DC} \tag{13}$$

On the other hand, the LCL filter is kept (despite having high cut-off frequency) as it maintains the dynamic interaction between the grid-side converter and the grid. Finally, the DC-link is modeled to represent the interaction between the inverter output active power P_o and the power generated by the PV array P_{PV} [29] as,

$$C_{dc}\frac{dV_{DC}}{dt} = \frac{P_{PV} - P_o}{V_{DC}} \tag{14}$$

B. Phasor to dq and Vice Versa

The inputs and outputs of the proposed phasor model are the phasor representation of the inverter output voltage $|V_{om}|\angle\theta_{vo}$ and output current $|I_{om}|\angle\theta_{io}$, respectively. Due to the reason explained before, the PLL block is removed in this step and the dq components of the output voltage are set as $V_{oq} = 0$ and $V_{od} = |V_{om}|$, based on the common assumption of building a dq reference frame of individual inverters presented in [26]. Therefore, the dq components of the phasor signal $f = |f_m|\angle\theta_f$ are given in (15), (16) (as the phasor to dq transformation), and the phasor representation of the f_d and f_q is obtained by (17)-(19) (as dq to phasor transformation).

$$f_d = |f_m|\cos\left(\theta_f - \theta_{vo}\right) \tag{15}$$

$$f_q = |f_m|\sin\left(\theta_f - \theta_{vo}\right) \tag{16}$$

$$|f_m| = \sqrt{f_d^2 + f_q^2} \tag{17}$$

$$\theta_f = \arctan\left(\frac{f_q}{f_d}\right) + \theta_{vo} \tag{18}$$

$$f = |f_m|\angle\theta_f \tag{19}$$

The output active and reactive powers of the inverter are obtained using (7), (8). As it can be seen from the model in Fig. 5, the DC-side components including MPPT, DC-link capacitor and its controller with the reactive power control loop are kept as the average model thereby maintaining the accuracy of PV system.

C. Mathematical Model in Phasor Domain

The complete mathematical model of the proposed-phasor based model is provided next. The mathematical model of DC-side comprised of the PV array model and DC-link dynamic

is given as,

$$I_{PV} = I_{ph} - I_0\left[\exp\left(\frac{(1-D)\,V_{DC} + I_{PV}\,R_s}{N_c V_T}\right) - 1\right] - \frac{(1-D)\,V_{DC} + I_{PV}\,R_s}{R_{sh}} \tag{20}$$

$$\frac{dV_{DC}}{dt} = \frac{1}{C_{dc}}\left(\frac{2\,I_{PV}(1-D)\,V_{DC} - V_{od}\,I_{od}}{2\,V_{DC}}\right) \tag{21}$$

where (20) is the current-voltage relationship of the single PV module expressed in (1) in which V_{PV} is substituted with $(1-D)\,V_{DC}$ from (13). Basing on (13) and (14), the equation of DC-link dynamic is obtained by (21).

The dynamics of these outer loops are expressed as,

$$I_{id}^{ref} = k_{p1}\,(V_{DC} - V_{DC}^{ref}) + k_{i1}\,\phi_d \tag{22}$$

$$\frac{d\phi_d}{dt} = V_{DC} - V_{DC}^{ref} \tag{23}$$

$$I_{iq}^{ref} = k_{p2}\,(Q_o - Q_{ref}) + k_{i2}\,\phi_q \tag{24}$$

$$\frac{d\phi_q}{dt} = Q_o - Q_{ref} \tag{25}$$

where k_{p1}, and k_{i1}, and ϕ_d are the corresponding gains and state of the PI controller in the DC-link voltage control loop. Similarly, k_{p2} and k_{i2} and ϕ_q are the corresponding gains and state of the PI controller in the reactive power control loop. Combining (8) with (24) and (25) results in,

$$I_{iq}^{ref} = k_{p2}\left(-\frac{V_{od}\,I_{oq}}{2} - Q_{ref}\right) + k_{i2}\,\phi_q \tag{26}$$

$$\frac{d\phi_q}{dt} = -\frac{V_{od}\,I_{oq}}{2} - Q_{ref} \tag{27}$$

The dq model of the output inductor L_g of the LCL filter in phasor domain is expressed as,

$$V_{od} - \frac{I_{iq}^{ref} - I_{oq}}{\omega_s\,C_f} = \omega_s\,L_g\,I_{oq} \tag{28}$$

$$V_{oq} + \frac{I_{id}^{ref} - I_{od}}{\omega_s\,C_f} = -\omega_s\,L_g\,I_{od} \tag{29}$$

Rewriting the equations (28) and (29) while replacing I_{id}^{ref} and I_{iq}^{ref} with their corresponding equations ((22) and (26)) gives the I_{od} and I_{oq} as,

$$I_{od} = -\frac{k_{p1}(V_{DC} - V_{DC}^{ref}) + k_{i1}\phi_d}{\omega_s^2 C_f L_g - 1} \tag{30}$$

$$I_{oq} = \frac{2V_{od}(\omega_s C_f) + k_{p2}(V_{od}I_{oq} + 2Q_{ref}) + 2k_{i2}\phi_q}{2\big(\omega_s^2 C_f L_g - 1\big)} \tag{31}$$

Finally, substituting the obtained I_o and I_q in the dq to phasor transformation (17)-(19), the inverter output current I_o which is injected to the common coupling point is obtained as,

$$I_o = \left|\sqrt{I_{od}^2 + I_{oq}^2}\right| \angle\, \arctan\left(\frac{I_{oq}}{I_{od}}\right) + \theta_{vo} \tag{32}$$

V. Model Validation

The efficacy and accuracy of the proposed phasor model is verified using a 5 kW residential two-stage single-phase PV system. The detailed and average models are employed for benchmarking purpose. The parameters of the residential PV system are given in Table I.

TABLE I
PV and Controller Parameters.

Component	Parameter	Value
PV Array	Photo current at STC, $I_{ph,STC}$	6.24 A
	Saturation current, $I_{0,STC}$	2.18e-12 A
	Series resistance, R_s	0.52 Ω
	Shunt resistance, R_{sh}	431 Ω
PV-side Converter	Rated power, P_{rated}	5 kW
	Rated DC voltage, V_{rated}	600 V
	Switching frequency, f_s	20 kHz
	PV-side capacitance, C_{PV}	4 μF
	DC-link capacitance, C_{DC}	1200 μF
	PV-side inductance, L_d	5 mH
Grid-side Converter	Rated power, S_{rated}	5 kW
	Rated AC voltage, V_{rated}^G	277 V
	System frequency, f	60 Hz
	Switching frequency, f_s	10 kHz
	LCL filter, L_i, C_f, L_g	2.6 mH, 8.64 μF, 1.5 mH
Volt-VAr Droop Setting	V_N	277 V
	Q_{max}, V_1,V_2	2.2 kVAr, 0.92 V_N, 0.98 V_N
	Q_{min}, V_3,V_4	-2.2 kVAr, 1.02 V_N, 1.08 V_N
Volt-Watt Droop Setting	P_{max}, V_1	5 kW, 1.06 V_N
	P_{min}, V_2	0, 1.1 V_N

A. Performance with Change in Solar Irradiance

Fig. 6(a) shows the solar irradiation variation used for the simulation, which goes down by two step changes from 1 p.u. to 0.5 p.u and then goes back to 1 p.u. The dynamic response of the output active power of the proposed phasor-based model is shown in Fig. 6(b) and is compared with the responses of detailed and average model. The maximum difference in active power obtained from the phasor-based model, average detail model, occurs when the irradiance is at maximum (1 p.u.) and are 0.95% and 0.34% between the phasor and detailed models, and the phasor and average models, respectively. The detailed model has the lowest active power output because of switching and resistive losses, which are ignored in average and phasor-based models.

B. Low Voltage Ride-Through (LVRT) Performance

According to IEEE 1547 [2], LVRT capability means that a smart inverter continues injecting current, based on the pre-disturbance operating point when the voltage drops in the low voltage ride-through operating region as shown in Fig. 7(a).

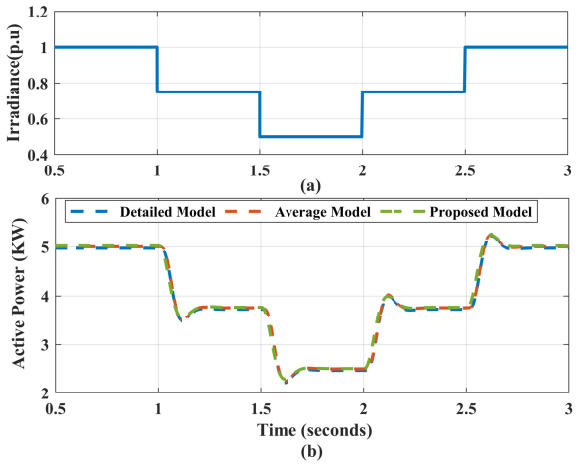

Fig. 6. Inverter response with varying solar irradiance: (a) irradiance profile, and (b) output active power.

Fig. 7 depicts the smart PV inverter performance during low-voltage and normal operation. The inverter is set to the Volt-VAr function mode based on the default droop setting for normal operating region as in [2]. Reactive power priority mode is considered for the simulation. As shown in Fig. 7, the smart inverter is injecting reactive power when the voltage sags (1-2.5 s) and is absorbing reactive power when the voltage swells (3-4 s), which mean that the inverter is able to provide dynamic voltage support to the grid during LVRT and normal operation. Moreover, due to reactive power priority, active power curtailment is enabled during reactive power injection and absorption as shown in Fig. 7(c). Fig. 7(d) represents the inverter output current. Not only does this case study verify the proper LVRT performance and Volt-VAr functionality of the designed smart PV inverter, it also demonstrates that the response from the proposed phasor-based model closely matches with that obtained from the detailed and average models.

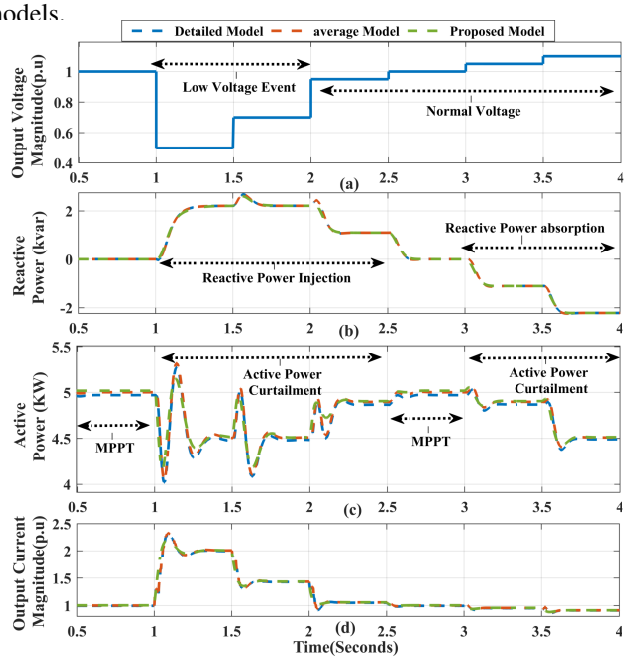

Fig. 7. Performance during LVRT: (a) inverter output Voltage magnitude (low voltage event and normal voltage), (b) output reactive power, (c) output active power, and (d) inverter output current magnitude.

TABLE II
SOLVE TIME OF THE DETAILED, AVERAGE, AND PHASOR-BASED MODEL FOR A 4-SECOND SIMULATION DURING LVRT.

Model	Step Size, μs	Solve Time, s	TDD, %
Detailed Model	0.25	568.5	1.3
Detailed Model	2	112.5	4.5
Detailed Model	5	78.3	12.5
Average Model	100	40	NA
Proposed Model	100	3.5	NA

C. Computational Performance

The execution time of LVRT case study of the all presented models for a 4 s simulation is summarized in Table II. The simulations are performed using MATLAB/Simulink R2019b in a PC with 2.9 GHz CPU and 16 GB RAM. The solver is set to ode4 (Runge-Kutta) with fixed step. Fast dynamics of the inner current loops (645 Hz bandwidth) and DC-side LC filter (1.125 kHz cut-off frequency) are neglected in the phasor model and the differential algebraic equations of the system are replaced with an algebraic set of equations of the current and voltage phasors at the grid frequency 60 Hz. The phasor model performs fastest, which is more than an order of magnitude faster than the average model and more than two orders of magnitude faster than the detailed model,as summarized in Table II. However, note that the step size used in the detailed model is in the range of 0.25- 2.0 μs in order to sufficiently capture the 20 kHz switching frequency of the boost converter. As summarized in Table II, total demand distortion (TDD) of the output current in the detailed model with Ts = 0.25 μs is 1.3%. However, with Ts = 5 μs, TDD is 12.5%, which violates limit prescribed in the IEEE 519-2014 [30]. Thus, we do not recommend solving the detailed model with sampling time above 2.0 μs. Moreover, as the time step used in average model and phasor-based model are the same, this clearly demonstrates the computational efficiency of the proposed phasor-based model. The efficiency of the proposed phasor-based model will be further illustrated in the next section using large-scale distribution grid.

VI. LARGE-SCALE SIMULATION

A. Simulation Setup

The application and scalability of the proposed model are demonstrated in this section using a modified feeder extracted from the IEEE 8500-node distribution feeder [31] with 400 smart PV inverters (each rated 5 kW), as shown in Fig. 8, operating on the dynamic voltage support modes (Volt-VAr and Volt-Watt). The split-phase transformers in the IEEE 8500-node [31] are replaced by regular two-winding transformers and PVs are connected on the LV side of the transformer at the load nodes. All PV systems are equipped with the smart inverters (S_{rated} = 5.028 kVA) with the Volt-VAr and Volt-Watt droop settings defined in the IEEE-1547 [2]. The models are developed in MATLAB/Simulink and solved using ePHASORSIM in offline mode. A fixed-step size of 0.1 ms is used.

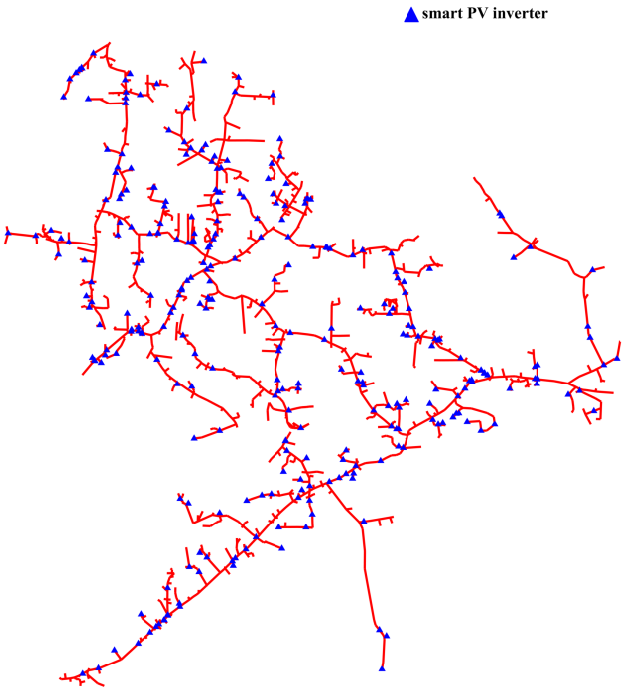

Fig. 8. Modified IEEE 8500-node distribution feeder along with 400 residential level smart PV inverters.

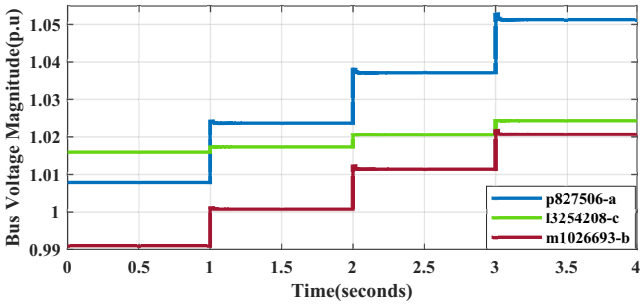

Fig. 9. Effect of PV penetration on the voltage profile.

B. Effect of PV Switching

The effect of PV switching on the grid voltage is investigated by integrating the proposed phasor-based model of the smart PV inverters to the mentioned distribution grid gradually (133 PVs in each second). The PV systems work on the MPPT mode and deliver maximum active power to the grid with zero reactive power (irradiance is at the maximum level). Fig. 9 depicts the voltage profile of three select buses.

C. Dynamic Volt-VAr Response

In this section, the dynamic Volt-VAr control (reactive power priority mode) of the proposed PV system model is evaluated in response to voltage change of the sub-station and with 100% irradiance level and 400 PVs. According to Fig. 1, there are five main regions in Volt-VAr characteristic of a PV system including maximum reactive power injection (V<V_1), injection droop (V_1<V<V_2), dead band (V_2<V<V_3), absorption droop (V_3<V<V_4), and maximum absorption (V_4<V) regions.

1) Volt-VAr Response with Sub-station Voltage Change: The sub-station voltage is varied as depicted in Fig. 10 (a), and the voltages, reactive powers and active powers of 10 selected

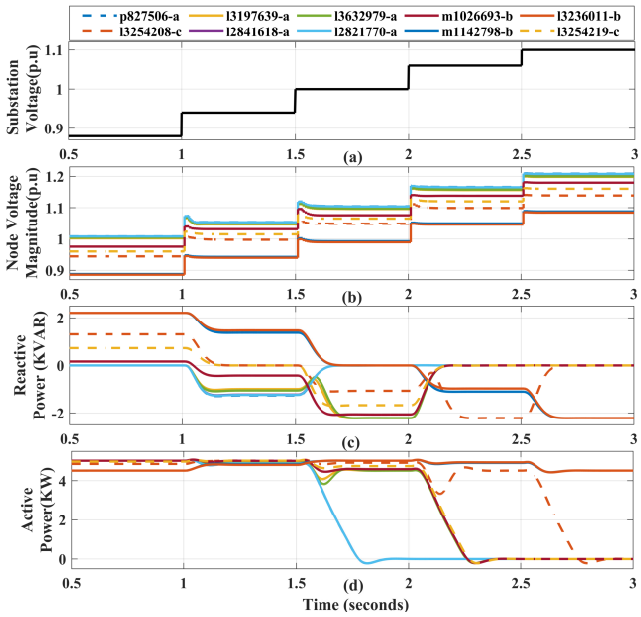

Fig. 10. Dynamic Volt-VAr performance under grid voltage change: (a) the sub-station voltage profile (normal operation mode), (b) output voltages of 10 selected PVs, (c) output reactive power of the 10 PVs, and (d) output active power of the 10 PVs.

PV buses are shown in Fig. 10 (b), (c), and (d), respectively. During 0.5-1 s, when the sub-station voltage is 0.88 p.u., the PVs connected to busses l3236011-b and m1142798-b and PVs connected to busses l3254208-c, 950-1c, and m1026693-b are operating on the maximum reactive power injection and injection droop regions, respectively; whereas, the other PVs are operating on the dead-band. Moreover, during this time interval, the reactive power of the PVs is obtained by the Volt-VAr droop characteristic based on their corresponding regions as shown in Fig. 10 (c). During the time interval 1-1.5 s, PVs connected to busses l3236011-b and m1142798-b and PV connected to busses l3254208-c and l3254219-c operate at injection droop and dead band regions, respectively; whereas the other PVs operate at the absorption droop region. During 1.5-2 s, the PVs connected to buses l3236011-b and m1142798-b, and the PVs connected to buses m1026693-b, l3254208-c and l3254219-c operate on dead-band and absorption droop, respectively, and the other PVs operate at the maximum absorption region. It is worth to note that since the voltages of the buses p827506-a,l2821770-a, and l2841618-a are greater than 1.1 p.u., the PVs at those buses inject no active and reactive power due to momentary cessation. Likewise, active power of the PVs follows Volt-Var characteristics and voltage ride-through requirements and curtail PV output as required due to reactive power priority mode.

2) Volt-VAr Response with Irradiance Change: Dynamic Volt-VAr response of the PV inverter with respect to change in irradiance is investigated in this case. Fig. 11(a) shows the solar irradiation variation used for the simulation, which goes down by a step change from 1 p.u. to 0.5 p.u and then goes back to 1 p.u. As it can be seen from Fig.11(a)-(d), during 0.5-1 s and 1.5-2 s, when the irradiance is 1 p.u, the rise in active power increases the node voltages. Therefore, most of the PVs operate at the reactive absorption droop region (except for the buses l3236011-b and m1142798-b) and absorb specified

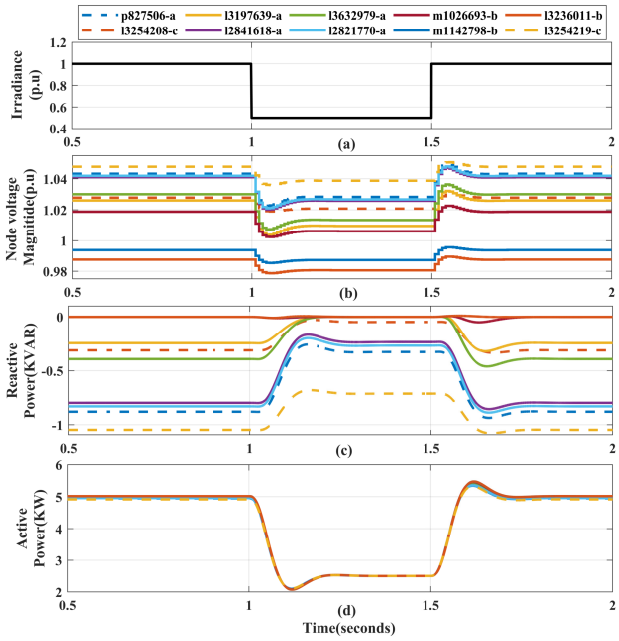

Fig. 11. Dynamic Volt-VAr response under irradiance change: (a) Irradiance profile, (b) voltages of the PV-connected buses, (c) output reactive power of the PVs, (d) output active power of the PVs.

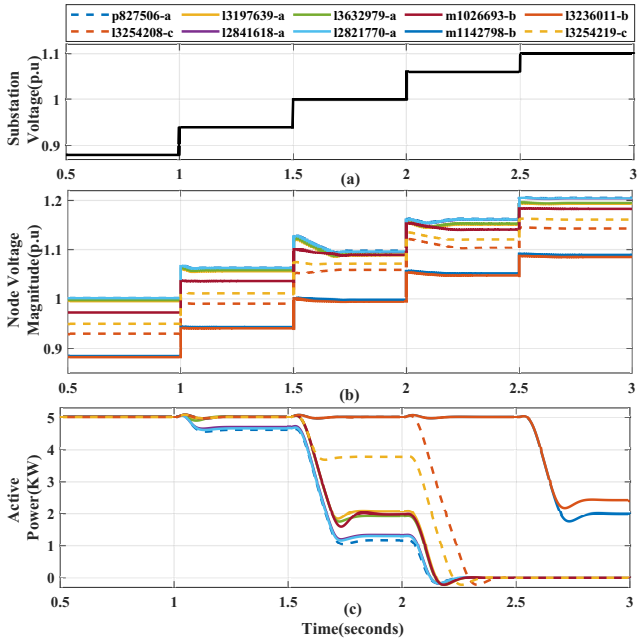

Fig. 12. Dynamic Volt-Watt function: (a) the grid voltage profile (normal operation mode), (b) voltages of the PV-connected buses, and (c) output active power of the PVs.

amount of reactive power obtained by their Volt-VAr droop characteristics. While during 1-1.5 s, when the irradiance level decreases to 0.5 p.u, the inverters output active powers are reduced as shown in Fig. 11(d). Subsequently, the increase in the node voltages is less than before, which results in less reactive power adsorption as shown in Fig.11 (c).

D. Dynamic Volt-Watt Response

The dynamic voltage support functionality of the smart PV inverters during over-voltage condition using Volt-Watt function is evaluated. To carry out this, the distribution grid with 400 smart PV inverters described in subsection VI-A is tested in response to voltage change of the sub-station as shown in Fig. 12 (a) and with 100% irradiance level. As Fig. 1, there are three main regions in Volt-Watt characteristic of a PV system including maximum active power region where the PV system works on MPPT mode (V<V_1), active power droop region (V_1<V<V_2), where the PV-side controller works on CPG mode and P_{ref} is obtained based on the Volt-Watt droop control), and minimum active power (V_2<V) region. The droop coefficients used in this case study, which are the default settings of IEEE 1547 [2], are given in Table I in the Appendix. To clearly investigate the performance of Volt-Watt function of the proposed model, output voltage and active power of PV at bus m1026693-b are discussed. As shown in Fig. 12(a)-(c), during 0.5-1.5 s, the bus voltage is smaller than V_1. Thus, the connected PV system works on the MPPT mode. In the time interval 1.5-2 s, the bus voltage lies on the active power droop region. Accordingly, the active power is curtailed to obtain P_{ref}=1.98 kW. During rest of the simulation, the bus voltage is greater than 1.1 p.u but smaller than 1.2 p.u; therefore, the PV temporarily ceases to operate.

E. Performance under Large Disturbance

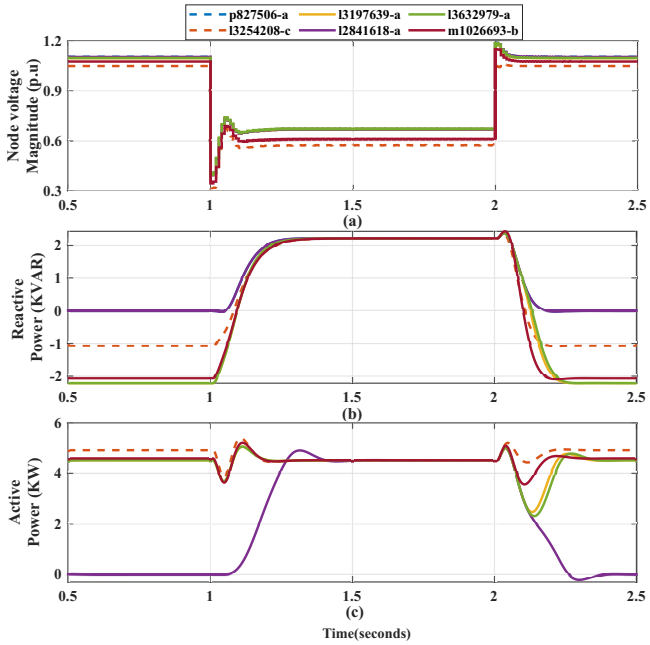

Fig. 13. PV system performance under large disturbance: (a) voltages of the impacted PV-connected buses, (b) output reactive power of the PVs, and (c) output active power of the PVs.

The dynamic performance of the proposed phasor model of the PV system under a power outage (as a large disturbance) is evaluated in this section. To do so, the line connecting bus l2841632 and regxfmr_190-8593 is disconnected at 1 s, and reconnected at 2 s. This event is significantly affecting the voltage and active/reactive powers of the PVs located on the islanded part of the grid (particularly at buses p827506-a, l3254208-c, l3197639-a, l2841618-a, l3632979-a, and m1026693-b) as shown in Fig. 13(a)-(c). For the PV connected at bus l3254208-c (dashed red curve in Fig. 13(a)-(c)), before

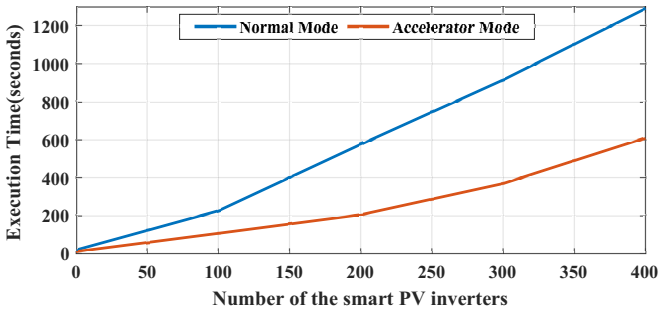

Fig. 14. Execution time of the phasor-based model with different number of smart PV inverters on the IEEE 8500-node Feeder.

the disturbance from 0.5 s to 1 s, the bus output voltage is 1.048 p.u. The reactive and active power of the PV system are Q_{ref}= -1.06 KVAr and P_{ref}= 4.91 kW, respectively, following the reference points of the absorption droop region. The bus voltage suddenly drops to 0.34 p.u. due to the line outage applied at 1 s causing significant dynamic in the reactive power response of the PV. The operating point changes from reactive power absorption mode to injection mode to support the voltage as set in Volt-VAr mode. This well explains the PV systems that operates in new set points in droop injection region which are Q_{ref}= 2.2 KVAr and P_{ref}= 4.51 kW. After disturbance is cleared at 2 s, the bus output at l3254208-c returns to its pre-disturbance value. For the PV connected to the bus l2841618-a (solid purple curve in Fig. 13(a)-(c)), before the disturbance (0.5 s to 1 s) as the voltage is 1.103 p.u., high-voltage momentary cessation is activated and its output powers are zero. While after line outage occurs at 1 s, its operating point is shifted to maximum reactive power injection region with Q_{ref}= 2.2 KVAr and P_{ref}= 4.51 kW. After fault is cleared at 2 s, the bus voltage returns to its pre-disturbance operating point. Please note that PV system was not designed with anti-islanding functions, which causes terminal voltage to dip around 0.6 p.u.

F. Computational Performance

The execution time of the previous case studies (dynamic Volt-Watt response for 3 s carried out in Section VI.D) is performed with 100, 200, 300, and 400 smart PV inverters connected to the modified IEEE 8500-node distribution grid. The simulations are performed on a PC with I7-10700H 2.90 GHz CPU and 16 GB RAM. The step size is chosen as 0.1 ms. The execution time of these cases is assessed in two modes of the simulator, i.e., normal and accelerator modes, and is summarized in Fig. 14. As seen in Fig. 14, the execution time with 400 PV inverters takes around 610 s in the accelerator mode and 1,250 s in the normal mode. The execution time as reported in [18] is 134 s for 1 s simulation (with 10 inverters, using a PC with comparable specification of Core I7-9850H 2.60 GHz CPU and 16 GB RAM, and step size of 2 ms). Using the proposed phasor-based model, 1 s simulation with 400 smart PV inverters with 0.1 ms step size can be solved in about 200 s. This clearly shows the computational efficiency of the proposed phasor-based model compared to the state-of-the-art [18].

VII. Conclusion

This paper presented an efficient and scalable phasor-based model of smart inverter for dynamic Volt/VAr and Volt/Watt analysis of large-scale distribution systems. The developed phasor-based model incorporates several control functions to fulfill the grid-code requirements, such as Volt/VAr control, Volt/Watt control, and LVRT function. The effectiveness of the proposed phasor-based model is demonstrated through the case studies carried out using a modified IEEE 8500-node distribution feeder with 400 distributed PVs. The comparative study shows that the developed phasor-based model significantly reduces the computational burden and it is applicable for the dynamic analysis of the distribution system with a large number of PV inverters. The results from the case studies show that the proposed model maintains a sufficient accuracy compared to the detailed and average models. Moreover, the proposed approach certainly overcomes the computational complexity of detailed and average models in solving dynamic simulation of large scale PV inveter-based systems. The application of the proposed model is intended for fast Volt/VAr and Volt/Watt dynamics at fundamental frequency. As the proposed model is developed only for a single frequency of interest, this can not be directly used for frequency-active power dynamics. We plan to develop dynamic phasor-based models suitable for frequency-active power dynamics as future work.

References

[1] "United states surpasses 2 million solar installations," Solar Energy Industry Associations.

[2] "IEEE standard for interconnection and interoperability of distributed energy resources with associated electric power systems interfaces," *IEEE Std 1547-2018 (Revision of IEEE Std 1547-2003)*, pp. 1–138, 2018.

[3] "EPIC 2.03a: Test Smart Inverter Enhanced Capabilities – Photovoltaics (PV)," Pacific Gas and Electric Company, Tech. Rep., 2019.

[4] H. V. Padullaparti, N. Ganta, and S. Santoso, "Voltage regulation at grid edge: Tuning of PV smart inverter control," in *Proc. IEEE PES Transmission and Distribution Conference and Exposition*, 2018, pp. 1–5.

[5] I. Roytelman, B. K. Wee, and R. L. Lugtu, "Volt/var control algorithm for modern distribution management system," *IEEE Transactions on Power Systems*, vol. 10, no. 3, pp. 1454–1460, Aug 1995.

[6] J. Rocabert, A. Luna, F. Blaabjerg, and P. Rodríguez, "Control of power converters in ac microgrids," *IEEE Transactions on Power Electronics*, vol. 27, no. 11, pp. 4734–4749, 2012.

[7] W. Sunderman, R. C. Dugan, and J. Smith, "Open source modeling of advanced inverter functions for solar photovoltaic installations," in *Proc. IEEE PES T&D Conference and Exposition*, 2014, pp. 1–5.

[8] S. Singh, S. Veda, S. P. Singh, R. Jain, and M. Baggu, "Event-driven predictive approach for real-time Volt/VAR control with CVR in solar PV rich active distribution network," *IEEE Transactions on Power Systems*, vol. 36, no. 5, pp. 3849–3864, 2021.

[9] E. Muljadi, M. Singh, and V. Gevorgian, "User guide for PV dynamic model simulation written on PSCAD platform," National Renewable Energy Lab. (NREL), Golden, CO, US., Tech. Rep., 2014.

[10] A. Nagarajan and R. Ayyanar, "Dynamic phasor model of single-phase inverters for analysis and simulation of large power distribution systems," in *Proc. 4th IEEE International Symposium on Power Electronics for Distributed Generation Systems*, 2013, pp. 1–6.

[11] X. Song, H. Cai, T. Jiang, T. Sennewald, J. Kircheis, S. Schlegel, L. Noris, Y. Benzetta, and D. Westermann, "Research on performance of real-time simulation based on inverter-dominated power grid," *IEEE Access*, pp. 1–1, 2020.

[12] V. Purba, S. V. Dhople, S. Jafarpour, F. Bullo, and B. B. Johnson, "Network-cognizant model reduction of grid-tied three-phase inverters," in *Proc. 55th Annual Allerton Conference on Communication, Control, and Computing*, 2017, pp. 157–164.

[13] L. Luo and S. V. Dhople, "Spatiotemporal model reduction of inverter-based islanded microgrids," *IEEE Transactions on Energy Conversion*, vol. 29, no. 4, pp. 823–832, 2014.

[14] V. Purba, S. V. Dhople, S. Jafarpour, F. Bullo, and B. B. Johnson, "Reduced-order structure-preserving model for parallel-connected three-phase grid-tied inverters," in *Proc. IEEE 18th Workshop on Control and Modeling for Power Electronics*, 2017, pp. 1–7.

[15] D. Venkatramanan and V. John, "Dynamic phasor modeling and stability analysis of SRF-PLL-based grid-tie inverter under islanded conditions," *IEEE Transactions on Industry Applications*, vol. 56, no. 2, pp. 1953–1965, 2020.

[16] Z. Shuai, Y. Peng, J. M. Guerrero, Y. Li, and Z. J. Shen, "Transient response analysis of inverter-based microgrids under unbalanced conditions using a dynamic phasor model," *IEEE Transactions on Industrial Electronics*, vol. 66, no. 4, pp. 2868–2879, 2019.

[17] Z. Miao, L. Piyasinghe, J. Khazaei, and L. Fan, "Dynamic phasor-based modeling of unbalanced radial distribution systems," *IEEE Transactions on Power Systems*, vol. 30, no. 6, pp. 3102–3109, 2015.

[18] W. Du, F. Tuffner, K. P. Schneider, R. H. Lasseter, J. Xie, Z. Chen, and B. P. Bhattarai, "Modeling of grid-forming and grid-following inverters for dynamic simulation of large-scale distribution systems," *IEEE Transactions on Power Delivery*, pp. 1–1, 2020.

[19] P. K. Pardhi, S. K. Sharma, and A. Chandra, "Control of single-phase solar photovoltaic supply system," *IEEE Transactions on Industry Applications*, vol. 56, no. 6, pp. 7132–7144, 2020.

[20] S. Shongwe and M. Hanif, "Comparative analysis of different single-diode PV modeling methods," *IEEE Journal of Photovoltaics*, vol. 5, no. 3, pp. 938–946, 2015.

[21] M. A. G. de Brito, L. Galotto, L. P. Sampaio, G. d. A. e Melo, and C. A. Canesin, "Evaluation of the main mppt techniques for photovoltaic applications," *IEEE Transactions on Industrial Electronics*, vol. 60, no. 3, pp. 1156–1167, 2013.

[22] A. Sangwongwanich, Y. Yang, and F. Blaabjerg, "High-performance constant power generation in grid-connected PV systems," *IEEE Transactions on Power Electronics*, vol. 31, no. 3, pp. 1822–1825, 2016.

[23] M. P. Zala, M. H. Pandya, K. N. Odedra, and D. P. Patel, "Active power control of PV system in MPPT and CPG mode," *Kalpa Publications in engineering*, vol. 1, pp. 270–277, 2017.

[24] E. I. Batzelis, G. Anagnostou, I. R. Cole, T. R. Betts, and B. C. Pal, "A state-space dynamic model for photovoltaic systems with full ancillary services support," *IEEE Transactions on Sustainable Energy*, vol. 10, no. 3, pp. 1399–1409, 2019.

[25] R. Zhang, M. Cardinal, P. Szczesny, and M. Dame, "A grid simulator with control of single-phase power converters in d-q rotating frame," in *Proc. 33rd Annual IEEE Power Electronics Specialists Conference*, vol. 3, 2002, pp. 1431–1436.

[26] N. Pogaku, M. Prodanovic, and T. C. Green, "Modeling, analysis and testing of autonomous operation of an inverter-based microgrid," *IEEE Transactions on Power Electronics*, vol. 22, no. 2, pp. 613–625, 2007.

[27] B. Guo, M. Su, Y. Sun, H. Wang, H. Dan, Z. Tang, and B. Cheng, "A robust second-order sliding mode control for single-phase photovoltaic grid-connected voltage source inverter," *IEEE Access*, vol. 7, pp. 53 202–53 212, 2019.

[28] Y. Gu, N. Bottrell, and T. C. Green, "Reduced-order models for representing converters in power system studies," *IEEE Transactions on Power Electronics*, vol. 33, no. 4, pp. 3644–3654, 2018.

[29] X. Mao and R. Ayyanar, "Average and phasor models of single phase pv generators for analysis and simulation of large power distribution systems," in *2009 Twenty-Fourth Annual IEEE Applied Power Electronics Conference and Exposition*, 2009, pp. 1964–1970.

[30] "IEEE recommended practice and requirements for harmonic control in electric power systems," *IEEE Std 519-2014 (Revision of IEEE Std 519-1992)*, pp. 1–29, 2014.

[31] K. P. Schneider, B. A. Mather, B. C. Pal, C.-W. Ten, G. J. Shirek, H. Zhu, J. C. Fuller, J. L. R. Pereira, L. F. Ochoa, L. R. de Araujo, R. C. Dugan, S. Matthias, S. Paudyal, T. E. McDermott, and W. Kersting, "Analytic considerations and design basis for the IEEE distribution test feeders," *IEEE Transactions on Power Systems*, vol. 33, no. 3, pp. 3181–3188, 2018.

Maryam Mahmoudi (S'19) received her B.S. degree from Amir Kabir University of Technology, Tehran, Iran, in 2009, and M.S. degree from Khaje Nasir Toosi University of Technology, Tehran, Iran, in 2012, both in Electrical Engineering. She is currently working toward the Ph.D. in Electrical Engineering with the ECE Department, Florida International University, Miami, FL, USA, as a Research Assistant. Her research interests include micro grids modeling and control; smart PV systems modeling and control; modeling and dynamic simulation of power systems with high penetration of power electronic converters; and real-time simulation.

Thai-Thanh Nguyen (S'15, M'19) received his B.S. in Electrical Engineering from Hanoi University of Science and Technology, Vietnam, in 2013, and his Ph. D. in Electrical Engineering, from Incheon National University, Korea, in 2019. From 2019 to 2020, he was a postdoctoral research associate at the Incheon National University. Since November 2020, he has been a postdoctoral research associate in Clarkson University, NY, USA. His research interests include power system control and stability, power converter control and the application of power electronics to power systems.

Tuyen Vu (S'13, M'16) received the B.S. degree in electrical engineering from the Hanoi University of Science Technology, Hanoi, Vietnam in 2012, and the Ph.D. in electrical engineering from Florida State University, Tallahassee, FL, USA, in 2016. From 2016 to 2017, he was a Postdoctoral Research Associate with the Center for Advanced Power Systems, Florida State University, where he was a Research Faculty from 2017 to 2018. Since July 2018, he has been an Assistant Professor with Clarkson University, Potsdam, NY, USA. His research interests include smart grid; power system dynamics, stability, and control; energy management and optimization; power systems cybersecurity, and integration of distributed energy resources into power systems.

Sumit Paudyal (S'07, M'12) received the B.E. degree from Tribhuvan University, Nepal in 2003, the M.Sc. degree from the University of Saskatchewan, Saskatoon, Canada, in 2008, and the Ph.D. degree from the University of Waterloo, Waterloo, Canada, in 2012, all in electrical engineering. He was a faculty member at Michigan Technological University, Houghton, MI, USA from 2012 to 2019. Since 2019, he is an Associate Professor in the Department of Electrical and Computer Engineering at Florida International University, Miami, FL, USA. His research interests include distribution grid modeling, dynamic studies, and optimization techniques in power systems.

Rob Hosvapian (SM'02) Rob Hovsapian received the M.S. degree in control and the Ph.D. degree in energy systems from the Mechanical Engineering Department, Florida State University, Tallahassee, FL, USA, in 1988 and 2009, respectively. He has spent more than 20 years working with Idaho National Laboratory, General Dynamics, TRW, and Northrop Grumman, as a Research Faculty with the Mechanical Engineering Department and as a Program Manager with the Office of the Naval Research, Center for Advanced Power Systems for the Electrical Ship Research and Development Consortium, Florida State University. He is currently working with the National Renewable Energy Laboratory, Golden, CO, USA, as a Research Advisor. He has a number of publications in the field of energy systems, thermodynamics optimization, thermal modeling, wind energy, and controls.